Dalton Transactions

ROYAL SOCIETY OF CHEMISTRY

PAPER

View Article Online
View Journal | View Issue

Cite this: *Dalton Trans.*, 2025, **54**, 14740

Tuning the ligand periphery in homoleptic Co(III) complexes: a versatile strategy to modulate electrocatalytic oxygen evolution reaction efficiency

Janardhanan Aiswarya, [a] Ragunath Madhu, [b,c] Ottoor Anitha, [a] Jan Grzegorz Malecki, [d] Subrata Kundu *[b,c] and Balasubramanian Murugesapandian *[a]

Received 17th July 2025,
Accepted 29th August 2025

DOI: 10.1039/d5dt01680k

rsc.li/dalton

In the relentless pursuit of sustainable energy solutions, the development of efficient, cost-effective, Earth-abundant molecular electrocatalysts is crucial. In this study, we report the design and synthesis of four new mononuclear Co(III) complexes (**C1**, **C2**, **C3** and **C4**) obtained through the reaction of Co $(CH_3COO)_2{\cdot}4H_2O$ with Schiff bases (**L1H$_2$**, **L2H$_2$**, **L3H$_2$**, and **L4H$_2$**) *via* aerial oxidation. Single-crystal X-ray diffraction (SCXRD) analysis confirms the formation of homoleptic mononuclear anionic Co(III) complexes $(\mathbf{L_2Co})^-$, with cationic triethylammonium as the counterion. The synthesized cobalt complexes demonstrate significant potential for catalyzing the oxygen evolution reaction (OER) in a 1 M KOH solution. All four complexes demonstrated promising electrocatalytic activity; however, complex "**C4**", comprising 2-amino-4-nitrophenol coupled with a 3-ethoxysalicylaldehyde ligand, exhibited superior performance. Notably, **C4** achieved a low overpotential of 340 mV at a current density of 10 mA cm^{-2}, along with a lower Tafel slope of 63 mV dec^{-1}, signifying rapid reaction kinetics. The outstanding catalytic efficiency of **C4** is attributed to a synergistic electronic effect resulting from the coexistence of electron-donating (EDGs) and electron-withdrawing groups (EWGs) in the ligand framework with the Co(III) ion, which enhances the charge transfer efficiency and stabilizes the active species during the catalytic cycle. Post-operational studies, including X-ray photoelectron spectroscopy (XPS) and scanning electron microscopy (SEM), were performed to evaluate the structural and morphological stability of complex **C4** after prolonged OER operation. Furthermore, this work could offer new insights into how electronic modifications on the ligand framework influence the catalytic efficiency of homoleptic Co(III) complexes in the OER.

Introduction

The overreliance on fossil fuels has resulted in rising carbon emission, global energy crises and accelerated climate change, causing severe environmental pollution. These challenges emphasize the urgent need to explore abundant, clean, and alternative sustainable energy sources.[1–3] To foster green and renewable energy, a key approach involves the electrochemical conversion of widely available molecules such as H_2O, CO_2 and N_2 into valuable chemical products utilizing sustainable energy resources.[4] Extensive research has been conducted on energy conversion technologies, including metal–air batteries, fuel cells, and electrochemical water splitting.[5,6] Electrochemical water splitting stands out as a promising solution for producing clean and renewable hydrogen fuel by splitting water into hydrogen and oxygen, where the hydrogen evolution reaction (HER) takes place at the cathode and the oxygen evolution reaction (OER) occurs at the anode.[7,8] Hydrogen generation through water electrolysis is regarded as an environmentally friendly and efficient approach.[9–12] However, the OER, which involves the transfer of four electrons and four protons, is hindered by a high theoretical overpotential of 1.23 V *vs.* the reversible hydrogen electrode (RHE) at 25 °C, which limits the overall efficiency of hydrogen production.[13–15] Due to its sluggish kinetics, the OER requires a high operating potential to achieve the necessary current densities for practical

[a]*Department of Chemistry, Bharathiar University, Coimbatore, 641046 Tamil Nadu, India. E-mail: mpandian@gmail.com, bmurugesapandian@buc.edu.in; Fax: +91-422-2422387; Tel: +91-422-2428312*
[b]*Materials Chemistry Laboratory for Energy, Environment and Catalysis, Electrochemical Process Engineering (EPE) Division, CSIR-Central Electrochemical Research Institute (CECRI), Karaikudi-630003, Tamil Nadu, India. E-mail: skundu@cecri.res.in, kundu.subrata@gmail.com; Fax: +91-4565-241487; Tel: +91-4565-241487*
[c]*Academy of Scientific and Innovative Research (AcSIR), Ghaziabad-201002, India*
[d]*Institute of Chemistry, University of Silesia, Szkolna 9, 40-006 Katowice, Poland*

applications.[16,17] Consequently, the development of highly efficient electrocatalysts to accelerate the reaction while minimizing the overpotential for the OER is crucial for enhancing the overall performance of water electrolysis systems.

RuO_2 and IrO_2 are widely recognized as state-of-the-art catalysts for the OER, offering excellent catalytic efficiency.[18–20] However, their scarcity hinders large-scale applications, driving the exploration of non-noble metal-based OER electrocatalysts. These alternatives aim to improve the thermodynamic and kinetic properties of catalytic reactions while ensuring cost-effectiveness, durability, and environmental sustainability. In recent years, significant progress has been made in designing advanced OER electrocatalysts with superior activity, reduced overpotential, and excellent stability under demanding operating conditions. As a result, several promising non-noble metal-based catalysts with exceptional efficiency and durability have been discovered, offering potential solutions for sustainable energy conversion. Earth-abundant metals such as Co, Ni, Mn, Cu and Fe are attracting significant interest in the development of cost-effective and efficient electrocatalysts for the water splitting reaction.[2,21–28]

Among Earth-abundant metals, cobalt (Co)-based catalysts have gained significant research interest due to their cost-effectiveness and natural abundance in the Earth's crust.[29] The distinct $3d^7 4s^2$ electronic configuration of cobalt facilitates multiple oxidation states, tunable redox behaviour, strong oxygen-binding affinity, and efficient electron-transfer dynamics.[27,29–31] These attributes make cobalt an effective catalyst for catalytic water splitting, particularly for the OER, where it often exhibits superior activity compared to noble metal-based systems under alkaline conditions. Furthermore, cobalt-based systems exhibit exceptional durability, enabling stable performance under highly alkaline environments and extreme electrochemical potentials, making them suitable for long-term electrolysis applications. A diverse range of cobalt-containing compounds, including oxides,[32–34] hydroxides,[35,36] sulphides,[37–39] phosphates/phosphides,[40–43] and nitrides,[44,45] have been extensively explored for heterogeneous OER catalysis, demonstrating high efficiency and stability. Alongside these materials, a variety of molecular cobalt complexes with well-defined structures have also been found to be efficient electrocatalysts for the OER in recent years.[46,47] The importance of molecular catalysts lies in the fact that their well-defined structures allow for a clear understanding of the detailed mechanism, enable rational tuning of the catalytic environment, and establish direct correlations between structural features and catalytic performance.[48]

In this field, Verani and co-workers reported a phenolate-rich Co(III) complex that exhibited excellent water oxidation activity, operating at a moderate overpotential of approximately 500 mV.[49] In 2016, Shi *et al.* reported a stable cobalt-based catalyst that achieved homogeneous electrocatalytic water oxidation in alkaline phosphate buffer, demonstrating high stability and a relatively low overpotential (η = 520 mV).[50] Also, Nath and co-workers synthesized a cobalt complex bearing a selenium-containing ligand, which demonstrated notable OER activity with an impressively low overpotential of 320 mV.[51] More recently, Sourav Das and co-workers reported a linear trinuclear cobalt complex featuring acetate bridges, exhibiting an overpotential of 380 mV.[46] The same group also developed a tetranuclear Co_4O_4 cubane-type complex, achieving efficient water oxidation at an overpotential as low as 325 mV.[47] Collectively, these studies underscore the growing potential of molecular cobalt-based architectures as efficient and tunable platforms for OER catalysis under mild conditions.

Metal complexes of aminophenol-salicylaldehyde-derived Schiff base ligands are well known in the literature, with applications spanning various fields.[52–54] However, their potential for electrocatalysis, specifically in the development of efficient catalysts for the OER, remains unexplored. Furthermore, the impact of electronic modifications on the ligand framework, particularly concerning the catalytic performance of cobalt complexes for the OER, has not been reported. The electronic nature of ligand substituents plays a crucial role in tuning the electrocatalytic behaviour of transition metal complexes. The incorporation of electron-donating and/or electron-withdrawing groups can significantly modulate the redox properties,[55] stability, and catalytic efficiency of electrocatalysts by influencing the metal center's electronic environment and the overall ligand field strength through a synergistic effect.

Motivated by the promising properties of cobalt coordination compounds as efficient OER electrocatalysts, we have synthesized and structurally characterized four new mononuclear Co(III) complexes (**C1**, **C2**, **C3** and **C4**) supported by aminophenol-coupled substituted salicylaldehyde Schiff base ligands with electronic modifications and studied their OER properties. The periphery of the ligands was systematically functionalized with electron-donating and electron-withdrawing groups to evaluate the synergistic effect on the OER catalytic performance of Co(III) complexes. Among the four complexes, **C4**, bearing an amino-nitrophenol and a 3-ethoxysalicylaldehyde framework, exhibited excellent electrocatalytic activity, achieving a low overpotential of 340 mV *vs.* RHE and a Tafel slope of 63 mV dec^{-1} under alkaline conditions (1 M KOH). Post-operational analyses, including XPS and SEM, confirmed the structural integrity and chemical robustness of **C4** under harsh anodic conditions. These findings indicate that the influence of electronic tuning around the ligand can enhance the electrocatalytic behaviour of Co(III) complexes, which may provide a basis for further molecular design of cobalt-based OER electrocatalysts.

Results and discussion

Synthetic methodology

To develop Co(III) complexes, we chose tridentate dianionic ligands ($\mathbf{L1H_2}$, $\mathbf{L2H_2}$, $\mathbf{L3H_2}$, and $\mathbf{L4H_2}$) bearing electronically tunable substituents at the periphery, and they can be readily synthesized by a condensation reaction from simple precursors. The reaction of 2-amino-substituted phenols (2-amino-4-methylphenol, 2-amino-4-nitrophenol) with the corresponding

substituted salicylaldehydes (3-methoxysalicylaldehyde, 3-ethoxysalicylaldehyde) resulted in the desired ligands with high yields. The synthetic pathway is depicted in Scheme S1 (SI). The synthesised ligands were purified and subsequently characterized using standard spectroscopic techniques, including Fourier-Transform Infrared (FT-IR) spectroscopy, UV–visible (UV–vis) spectroscopy, and Nuclear Magnetic Resonance (NMR) spectroscopy. A comprehensive synthetic procedure and detailed spectroscopic data are presented in the Experimental section and the SI (Fig. S1–S16).

The ^{1}H NMR spectra of the ligands **L1H$_2$–L4H$_2$** exhibited the characteristic signals for the imine (–CH═N–) protons at δ 8.95, 8.95, 9.09, and 9.10 ppm, respectively. In the case of **L1H$_2$** and **L2H$_2$**, the methyl (–CH_3) protons appeared at δ 2.25 ppm, while the methoxy (–OCH_3) protons resonated at δ 3.80 ppm (**L1H$_2$**) and δ 3.82 ppm (**L3H$_2$**). The presence of the ethoxy (–OCH_2CH_3) group was confirmed by a quartet at δ 4.06 ppm for **L2H$_2$** and at δ 4.08 ppm for **L4H$_2$**, corresponding to the –CH_2 protons, while the methyl (–CH_3) protons of the ethoxy group appeared as a triplet at δ 1.34 ppm (**L2H$_2$**) and δ 1.35 ppm (**L4H$_2$**). The hydroxyl (–OH) protons of the 2-amino-R-phenol (R = methyl, nitro) moiety appeared at δ 9.55 ppm for **L1H$_2$** and **L2H$_2$** and at δ 11.42 ppm for **L3H$_2$** and **L4H$_2$**. Additionally, the hydroxyl (–OH) protons of the substituted salicylaldehyde moiety were observed at δ 14.13 ppm for **L1H$_2$**, δ 14.18 ppm for **L2H$_2$**, δ 13.41 ppm for **L3H$_2$** and δ 13.46 ppm for **L4H$_2$**. The aromatic protons resonated in the ranges of δ 7.20–6.82 ppm (**L1H$_2$** and **L2H$_2$**) and δ 8.28–6.76 ppm (**L3H$_2$** and **L4H$_2$**). The ^{13}C NMR spectra exhibited expected signals at the respective regions, and the imine (–CH═N–) carbon appeared at δ 161.18 ppm (**L1H$_2$**), 161.16 ppm (**L2H$_2$**), 164.48 ppm (**L3H$_2$**), and 164.56 ppm (**L4H$_2$**), respectively. The ^{1}H and ^{13}C NMR spectra are presented in Fig. S1–S8. The FT-IR spectra of the ligands exhibited characteristic $\nu_{C=N}$ stretching bands at 1622 cm^{-1} (**L1H$_2$**), 1612 cm^{-1} (**L2H$_2$**), 1639 cm^{-1} (**L3H$_2$**), and 1639 cm^{-1} (**L4H$_2$**) (Fig. S9–S12).[56] The UV-vis spectra of the ligands exhibit absorption maxima (λ_{max}) at 274 and 347 nm (**L1H$_2$**), 274 and 349 nm (**L2H$_2$**), 225 and 288 nm (**L3H$_2$**), and 223 and 270 nm (**L4H$_2$**), which correspond to π–π^*/n–π^* electronic transitions and charge transfer transitions, respectively (Fig. S13–S16).[57] These spectral features confirm the successful formation of the ligands and the presence of key functional groups. The ligands (**L1H$_2$–L4H$_2$**) were reacted with $Co(CH_3COO)_2{\cdot}6H_2O$ in the presence of excess triethylamine (TEA) in a 2 : 1 molar ratio in methanol or an acetonitrile–methanol mixture under aerobic conditions, followed by slow evaporation, yielding brown-coloured crystals of complexes **C1–C4** of ligands **L1H$_2$**, **L2H$_2$**, **L3H$_2$**, and **L4H$_2$**, respectively, as illustrated in Scheme 1. The synthesized four new Co(III) complexes were characterized using FT-IR spectroscopy, UV-vis spectroscopy, ^{1}H NMR spectroscopy, and high-resolution mass spectrometry (HRMS) (Fig. S17–S28). Furthermore, the molecular structures of the complexes were confirmed by single-crystal X-ray diffraction analysis.

The observation of a ^{1}H NMR signal in the diamagnetic region for the metal complexes (**C1–C4**) supports that the cobalt complexes are diamagnetic in nature and that the Co ion is present in the +3 oxidation state. The disappearance of the –OH proton signal in the ^{1}H NMR spectra of the four complexes suggests that the hydroxyl group has been deprotonated and coordinated to the cobalt center, resulting in the formation of a stable metal–ligand bond. The imine proton (–CH═N–) signal was observed at δ 8.84 ppm (**C1**), δ 8.87 ppm (**C2**), δ 9.10 ppm (**C3**), and δ 9.28 ppm (**C4**). Additionally, slight shifts were observed in the aromatic, aliphatic, and imine (–CH═N) proton signals, further supporting complex formation. In **C1**, the triplet signal observed at δ 1.00 ppm was assigned to the methyl (–CH_3) protons of the triethylammonium ion. The broad signal around δ 3.78 ppm corresponds to the ethyl (–CH_2–) protons of the triethylammonium ion, which merged with the –OCH_3 protons of the *o*-vanillin moiety. Furthermore, the broad resonance at δ 2.71 ppm was attributed to the –NH– proton of the triethylammonium ion, confirming its incorporation into the complexes. The intensity ratio of the imine proton signal to the methyl proton signals of the triethylammonium cation supports the presence of two Schiff base ligands and one triethylammonium cation in all the complexes (Fig. S17–S20). Furthermore, the FT-IR spectra of the complexes suggest that, upon coordination with cobalt, the imine bands (–CH═N–) exhibited a shift to lower frequencies to 1599 cm^{-1} (**C1**), 1599 cm^{-1} (**C2**), 1612 cm^{-1} (**C3**), and 1605 cm^{-1} (**C4**), compared to those observed in free ligands (Fig. S21–24). This spectral shift indicates a reduction in the bond strength of the C═N bond, attributed to the withdrawal of electron density by the cobalt ion, thereby confirming coordination of the imine nitrogen to the Co(III) ion. Additionally, UV–vis spectral data (Fig. S13–S16) further support the formation of the cobalt complexes: upon complexation with the cobalt metal center, the absorption maxima of the resulting complexes were observed at 246 nm (**C1**), 258 nm (**C2**), 257 nm (**C3**), and 258 nm (**C4**), indicating the ligand based π–π^*/n–π^* transition. Furthermore, all four Co(III) complexes exhibit additional low-energy absorption bands at 433 nm (**C1**), 447 nm (**C2**), 423 nm (**C3**), and 426 nm (**C4**), characteristic of ligand-to-metal charge transfer (phenoxo to Co(III)) transition, which is absent in the free ligands.[58,59] Moreover, the molecular ion peaks observed in the HRMS spectra of complexes **C1–C4** (Fig. S25–28) are as follows: **C1** at *m*/*z* 707.1021, **C2** at *m*/*z* 735.1625, **C3** at *m*/*z* 751.1456, and **C4** at *m*/*z* 762.5750. These values are in good agreement with the expected molecular masses, confirming the molecular compositions of the synthesized compounds.

Description of X-ray crystal structures

The single crystals of complexes **C1** and **C2** were obtained from methanol *via* slow evaporation, whereas those of **C3** and **C4** were obtained from slow evaporation of a 1 : 1 mixture of acetonitrile and methanol. Single-crystal X-ray diffraction analyses were performed for all four Co(III) complexes (**C1–C4**), whose molecular structures are depicted in Fig. 1a–d, with thermal ellipsoids drawn at the 50% probability level. Complex **C1** crystallized in the triclinic crystal system with the $P\bar{1}$ space

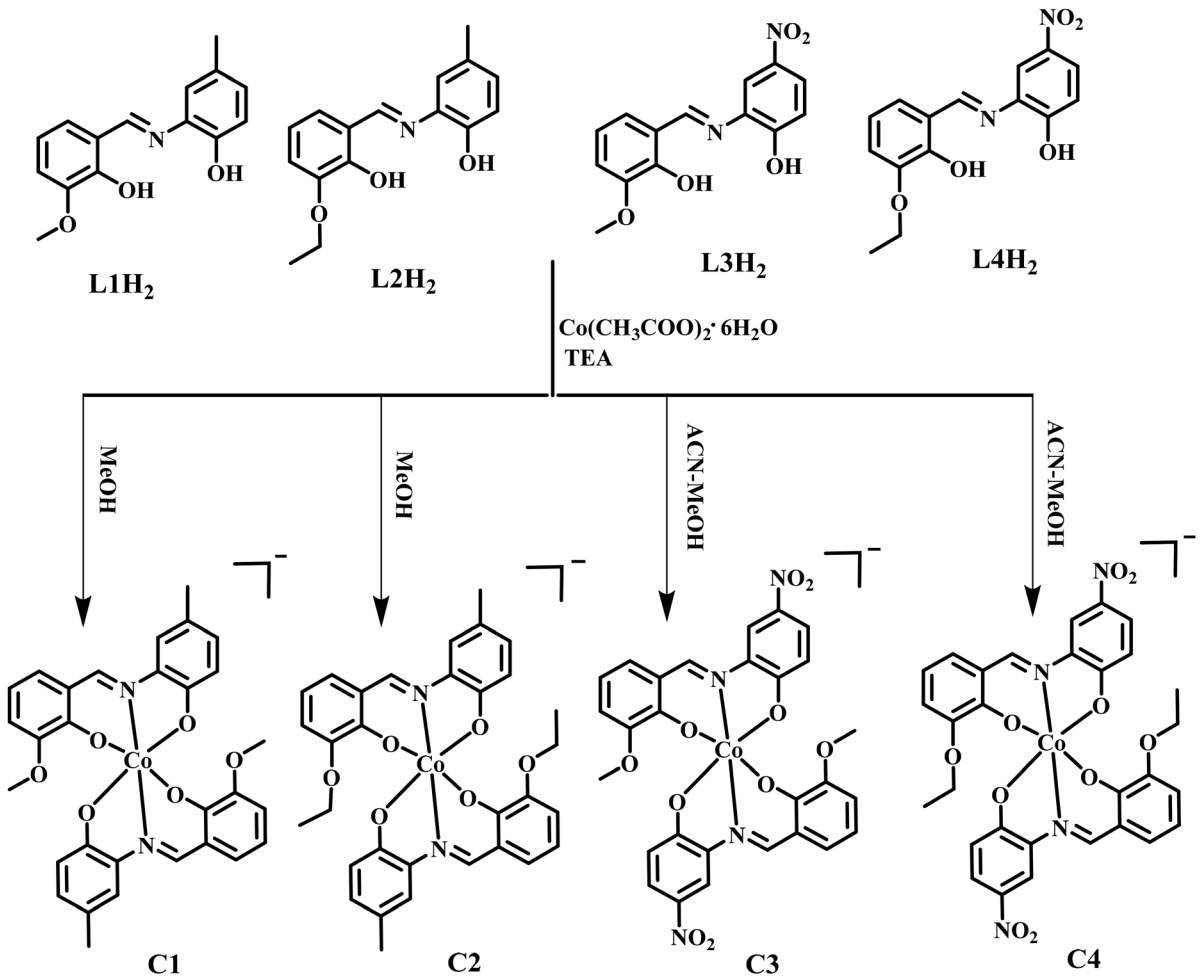

Scheme 1 Synthesis of Co(III) complexes (**C1–C4**) [counter triethylammonium cations have been omitted for clarity].

group, whereas **C2** adopts the orthorhombic $Pna2_1$ space group. Both **C3** and **C4** belong to the monoclinic $P2_1/n$ space group. The crystallographic analysis indicates the homoleptic feature of the complexes, and the asymmetric unit of each complex consists of a mononuclear anionic moiety, $[L_2Co]^-$, along with a triethylammonium cation and solvent molecules. The cobalt center in all complexes adopts a distorted octahedral geometry, and it is surrounded by two tridentate doubly deprotonated ligands with –ONO– chelation around the Co(III) ions (Fig. 1e) *via* two phenolic oxygen atoms from substituted salicylaldehyde moieties, two phenolic oxygen atoms from 2-amino-substituted phenol units, and two nitrogen atoms from imine groups. The Co–O bond lengths involving aminophenol-derived phenolic oxygen (Co–O_{pham}) are in the range of 1.894–1.927 Å, while those involving aldehyde-derived phenolic oxygen (Co–O_{phal}) lie between 1.880 and 1.894 Å, as listed in Table 1. Key bond angles include O_{al}–Co–O_{am} (al: aldehydic part, am: amine part), which are 177.37°, 177.70°, 177.90°, and 178.97° for **C1–C4**, respectively. The O_{al}–Co–O_{al} angles are 90.84°, 91.50°, 90.50°, and 89.48°, while the O_{am}–Co–O_{am} angles are 88.30°, 88.60°, 88.40°, and 92.60°, respectively (Table S2). The homoleptic complexes **C1** and **C2** co-crystallize with two water molecules, **C3** with one, and **C4** contains no water molecules. Crystallographic refinement parameters and full structural data are detailed in Tables S1 and S2, with CCDC deposition numbers as follows: **C1** (2450219), **C2** (2450220), **C3** (2450221), and **C4** (2450222).

The Co atoms in all four complexes were determined to be in the +3 oxidation state, as supported by Bond Valence Sum (BVS) calculations. The corresponding BVS values are provided in Table 2, with a detailed summary of the calculations included in Table S3.

Electrocatalytic OER performance of Co complexes in 1 M KOH solution

The as-synthesized Co-based **C1**, **C2**, **C3** and **C4** complexes are tested for the OER in 1 M 'Fe-free' KOH using a conventional three electrode system, with Hg/HgO as the reference, modified carbon cloth (CC) as the working and a Pt ring as the counter electrode. Linear sweep voltammetry (LSV) at a scan rate of 5 mV s^{-1} was performed to evaluate the catalytic activity of all four complexes. The resulting LSVs, with 60% *iR* com-

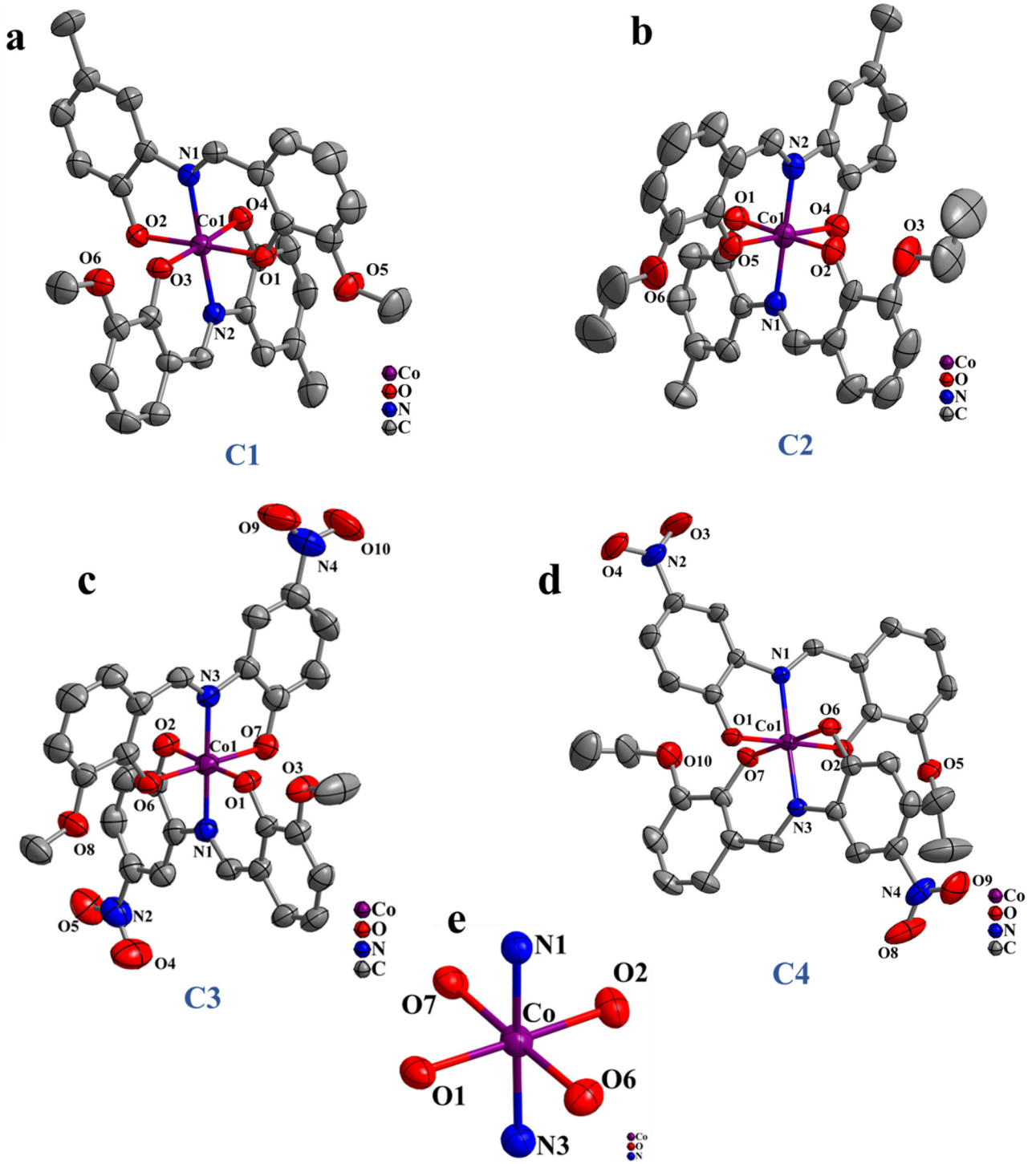

Fig. 1 (a–d) Molecular structures of homoleptic Co(III) complexes **C1–C4** with ellipsoids at 50% probability. Hydrogen atoms and counter cations are omitted for clarity. (e) A representative example of the coordination environment around the Co centre in **C4**.

pensation, shown in Fig. 2a demonstrate that **C4** exhibits superior OER performance, requiring an overpotential of only 340 mV to achieve a benchmarking current density of 10 mA cm^{-2}. The catalysts **C3**, **C2** and **C1** required 362, 370 and 390 mV to attain the same benchmarking current density, respectively. For comparison, LSV polarization of bare CC is provided in Fig. 2a. Furthermore, electrochemical impedance spectroscopy (EIS) was carried out to analyze the resistance exhibited by the Co-complexes towards electron transfer at the electrode–electrolyte interface during the OER process. The EIS results in Fig. 2b imply that **C1**, **C2**, **C3** and **C4** possess R_{ct} (charge transfer resistance) values of 3.03, 2.85, 2.77 and

Table 1 Selected bond distances of **C1–C4**

Selected bond distance of **C1**		Selected bond distance of **C2**	
Bonds	Bond distance(Å)	Bonds	Bond distance(Å)
Co1–O2	1.927(2)	Co1–O1	1.903(4)
Co1–O3	1.878(2)	Co1–O2	1.890(4)
Co1–O1	1.890(2)	Co1–O4	1.907(4)
Co1–O4	1.889(2)	Co1–O5	1.894(4)
Co1–N2	1.896(2)	Co1–N1	1.902(5)
Co1–N1	1.890(2)	Co1–N2	1.889(5)
Selected bond distance of **C3**		Selected bond distance of **C4**	
Bonds	Bond distance(Å)	Bonds	Bond distance(Å)
Co1–O1	1.881(3)	Co1–O1	1.903(2)
Co1–O2	1.910(3)	Co1–O2	1.883(2)
Co1–O6	1.880(3)	Co1–O6	1.894(2)
Co1–O7	1.912(3)	Co1–O7	1.894(2)
Co1–N1	1.900(3)	Co1–N1	1.896(2)
Co1–N3	1.893(3)	Co1–N3	1.896(2)

Table 2 Bond valence sum calculations[a] for determining the oxidation of the Co atoms in **C1–C4**[b]

	C1	**C2**	**C3**	**C4**
Co(II)	3.36	3.27	3.30	3.30
Co(III)	3.36	3.22	3.33	3.35

[a] The value that is underlined is the one closest to the charge for which it was calculated. [b] The oxidation state of the cobalt atom is the nearest whole number to the underlined value.

2.58 Ω, suggesting that the **C4** complex with the lowest R_{ct} exhibits less resistance towards the electron transfer at the interface, respectively. The higher activity of **C4** was evident from the overpotential comparison at different current densities (10 and 30 mA cm^{-2}), as portrayed in Fig. S29a. The bar diagram evidences that even at varying current (high) densities, the **C4** complex shows superior catalytic performance, outperforming other Co-complexes. Furthermore, the OER performance of the Co-complexes was compared with that of commercial RuO_2 (Fig. S29b). Impressively, the **C4** complex outperformed the commercial catalyst, exhibiting superior activity compared to RuO_2, with an overpotential of 360 mV to reach the 10 mA cm^{-2} current density. To further investigate the electrode–electrolyte interface kinetics, Tafel slope analysis was performed on the *iR*-corrected LSV polarization results (Fig. 2c). The resulting Tafel slopes for **C1**, **C2**, **C3**, and **C4** are 95, 71, 68 and 63 mV dec^{-1}, respectively. The lowest Tafel slope observed for **C4** indicates faster electron transfer kinetics at the interface, which contributes to its superior OER performance compared to the other Co complexes. The long-term stability of the **C4** catalyst was evaluated using chronopotentiometry at a constant potential of 1.60 V *vs.* RHE. The results in Fig. 2d demonstrate stable performance of **C4** for 26 h, with only a minimal decrease in the applied potential, indicating good durability in 1 M KOH solution.

In order to gain a deeper understanding of the intrinsic electrocatalytic activity, the surface area of the catalysts was determined using the reduction peak from the redox region (Fig. S30a–d). The complex **C4** exhibited the high reduction

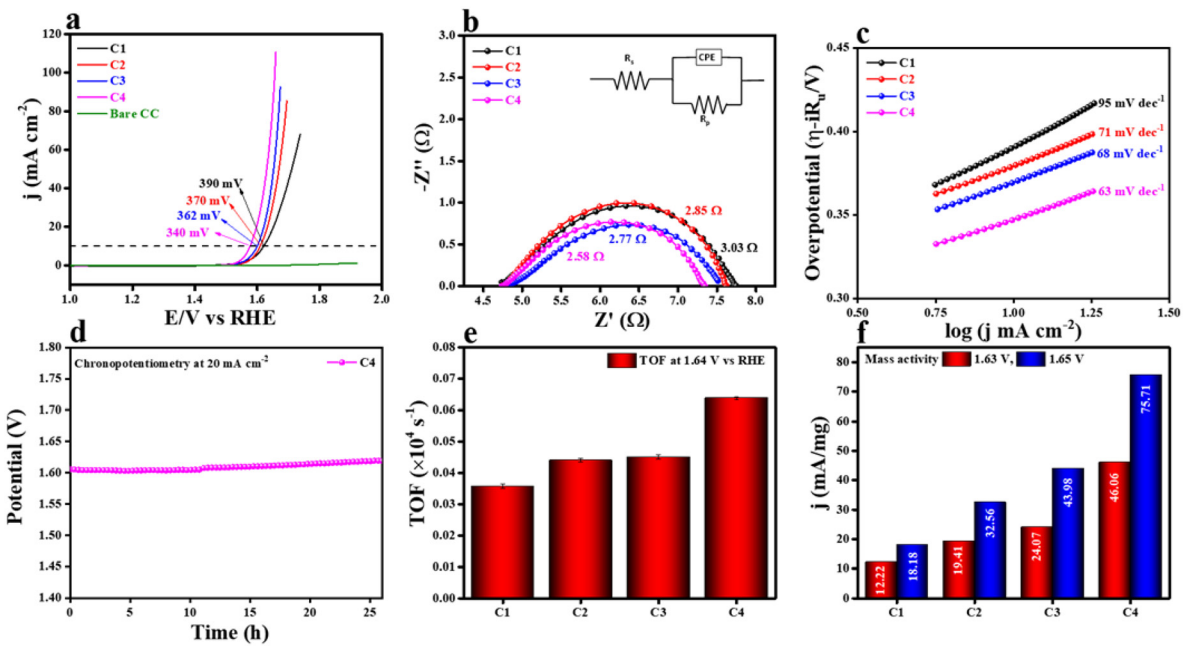

Fig. 2 Electrocatalytic OER performance: (a) the geometrically normalized LSV results for **C1**, **C2**, **C3**, **C4** and bare **CC** at 10 mA cm^{-2} current density; (b) electrochemical impedance spectra (Nyquist plot) of **C1**, **C2**, **C3** and **C4** at 1.674 V (*vs.* RHE). (c) Corresponding computed Tafel slopes from the *iR* drop-free LSV curves; (d) chronopotentiometric analysis of **C4** at 20 mA cm^{-2} current density for 26 h; (e) TOF values of **C1**, **C2**, **C3** and **C4** obtained at 1.64 V *vs.* RHE; (f) mass-dependent activity of **C1**, **C2**, **C3** and **C4** at 1.63 V and 1.65 V *vs.* RHE.

surface area (0.0002508 V A), compared to **C3** (0.0001962 V A), **C2** (0.0001438 V A) and **C1** (0.00007359 V A), suggesting that more surface active sites are available for adsorption of OH^-, which subsequently boosts the OER performance. Moreover, **C4** possesses high charge (0.02508 C) accumulated over the electrode surface towards the facile adsorption of OH^- ions (Fig. S31). The higher charge of **C4** over the electrode is the primary reason for its better OER performance than the other Co complexes. Furthermore, to gain insights into the intrinsic activity, turnover frequency (TOF) values were calculated based on the reduction area (Fig. S30). As expected from Fig. 2e, **C4** demonstrated the highest TOF value (0.06388×10^4 s^{-1}), followed by **C3** (0.0451×10^4 s^{-1}), **C2** (0.04407×10^4 s^{-1}) and **C1** (0.03577×10^4 s^{-1}). This indicates that **C4** generates more oxygen molecules per active site per second, which signifies superior catalytic activity compared to the other Co-complex catalysts. In addition to intrinsic analysis, mass-dependent activity was studied by normalizing the current density with the catalyst loading, and the obtained LSV results are provided in Fig. S32. The mass-normalized LSV confirms the same activity trend as observed in the geometric LSV results. Further analysis at 1.63 V and 1.65 V *vs.* RHE (Fig. 2f) revealed that **C4** displayed significantly higher mass activities of 46.06 and 75.71 mA mg^{-1}, respectively, than other cobalt complexes, demonstrating its superior intrinsic catalytic performance. Again, to validate the higher performance of the **C4** complex, the electrochemically active surface areas (ECSAs) of the catalysts were determined by performing cyclic voltammetry (CV) measurements at an applied potential of 0.1–0.2 V *vs.* Hg/HgO at various scan rates in the non-faradaic region (Fig. S33a–d). Double-layer capacitance (C_{dl}) values were determined by calculating the slope of the linear fit to the cathodic and anodic current densities obtained from the CV, as shown in Fig. S33e. The determined C_{dl} values are higher for **C4** (9.73 mF) than for **C1** (2.15 mF), **C2** (3.84 mF), and **C3** (5.32 mF), suggesting that the higher capacitance is owing to the greater number of charge species (OH^-). Using the formula ECSA = C_{dl}/C_s (where C_s is the specific capacitance of a flat electrode, assumed to be 0.04 mF cm^{-2}), the ECSA values were calculated to be 53.75, 96, 133 and 243.75 cm^2 for **C1**, **C2**, **C3** and **C4**, respectively. The higher ECSA of **C4** suggests a higher number of accessible active sites available for the OER, which contributes to its enhanced catalytic activity. Finally, apart from long-term stability, dynamic stability of the **C4** catalyst was tested by accelerated degradation (AD) studies. The catalyst was subjected to continuous 1000 CV cycles at a scan rate of 150 mV s^{-1} in 1 M KOH solution. Following the AD study, LSV and electrochemical impedance spectroscopy (EIS) measurements were conducted. The LSV results (Fig. S34a) show a slight decrease in activity, with a 9 mV increase in overpotential (to 349 mV) to reach a current density of 10 mA cm^{-2}. Similarly, the EIS analysis (Fig. S34b) reveals a slight increase in charge transfer resistance (R_{ct}) from 2.58 Ω to 2.76 Ω, indicating marginally slower electron transfer kinetics at the interface. The observed slight decrease in activity over multiple CV cycles is likely attributed to the reduction in charge accumulated on the catalyst's active surface area.[60,61] This diminished charge accumulation may hinder the dissociation of water molecules and the subsequent adsorption of hydroxide ions (OH^-), which are crucial steps in the OER process. The superior OER performance of **C4**, relative to **C1**, **C2**, and **C3**, can be attributed to the synergistic interaction between electron-donating and electron-withdrawing substituents within the ligand framework and the Co(III) center. This electronic interplay fine-tunes the local electronic environment around the metal center, thereby enhancing catalytic activity. Notably, both **C3** and **C4** exhibit lower overpotentials than **C1** and **C2**, which is likely attributable to the presence of both types of substituents in their ligand scaffolds. Among the studied analogues, complexes bearing ethoxy groups ($-OCH_2CH_3$) consistently exhibited lower overpotentials and enhanced catalytic activity compared to their methoxy-substituted ($-OCH_3$) counterparts.[55] This improvement is primarily ascribed to the ethoxy group's pronounced inductive electron-donating effect, facilitated by its extended alkyl chain. The increased electron donation enhances the electron density at the Co center, thereby stabilizing Co–OOH intermediates, which play a pivotal role in the OER pathway. The electron-donating groups facilitate electron transfer to the Co center, whereas the electron-withdrawing groups contribute to stabilizing the resulting charge distribution in **C4**. This cooperative effect plays a crucial role in minimizing the overpotential and enhancing catalytic efficiency. These observations underscore the significance of strategic ligand design, importantly, the incorporation of complementary electronic substituents as an effective approach for modulating the redox behaviour, electronic structure, and catalytic performance of cobalt-based complexes. Furthermore, such electronic modulation can result in a more favorable alignment of molecular orbitals, improving electron transfer rates and reducing the overpotential required for catalytic turnover.[55,62] The structural robustness and stability of complex **C4** before and after the OER were examined using X-ray photoelectron spectroscopy (XPS), scanning electron microscopy (SEM), powder XRD, UV-vis spectroscopy and FT-IR spectroscopy. The XPS spectra of the **C4** sample before the OER are presented in Fig. S35. The Co 2p spectrum (Fig. S35a) exhibits spin–orbit split peaks at binding energies of 780.84 eV (Co $2p_{3/2}$) and 795.68 eV (Co $2p_{1/2}$), characteristic of the Co ion in the +3 oxidation state.[63] The O 1s spectrum (Fig. S35b) reveals three characteristic peaks located at 530.54 eV, 531.87 eV, and 533.72 eV, corresponding to Co–O bonds, C–O species, and adsorbed water molecules, respectively. The N 1s region (Fig. S35c) shows peaks at 399.04 eV and 400.25 eV, attributed to C=N functionalities and Co–N bonding, respectively, whereas peaks at 404.41 eV and 406.30 eV correspond to N–O and N=O groups from the aromatic nitro substituent.[64] The deconvoluted C 1s spectrum (Fig. S35d) indicates the presence of C–C/C=C (284.1 eV), C–O (285.36 eV), and C–NO_2 (288.6 eV) functionalities. The post-OER XPS analysis of the **C4** sample is presented in Fig. S36. The Co 2p spectrum (Fig. S36a) retains features indicative of Co(III), with a positive shift of 0.32 eV to 781.16 eV for the $2p_{3/2}$ peak and the corresponding $2p_{1/2}$ peak

at 796.13 eV, consistent with the formation of catalytically active Co-based species during the OER. The O 1s spectrum (Fig. S36b) shows peaks at 531.42 eV (Co–O) and 532.58 eV (C–O). The N 1s region (Fig. S36c) continues to show C=N (399.52 eV), Co–N (400.25 eV), and nitro group signals at 404.5 eV (N–O) and 406.5 eV (N=O). The C 1s spectrum (Fig. S36d) reveals distinct peaks at 284.4 eV (C–C/C=C), 285.44 eV (C=N), and 288.73 eV (C–O), confirming the presence of key functional groups of the ligand in the post-OER **C4** sample. The negligible changes in binding energies and the preservation of peak features indicate that the structural integrity is maintained even after long-term OER operation. Furthermore, the SEM images (Fig. S37) further confirm the morphological stability of **C4**. Both the pristine and post OER-cycled samples exhibit a similar irregular flake-like morphology. In addition, the powder XRD patterns of the simulated, experimental and post-OER samples (Fig. S38) remain almost identical, confirming their structural integrity. The UV–vis spectra (Fig. S39) also show negligible changes, with the retention of characteristic ligand-to-metal charge transfer and π–π^*/n–π^* absorption bands, suggesting that the electronic environment around the Co centers is preserved after the OER. Similarly, the FT-IR spectra (Fig. S40) of the complex before and after the OER exhibit consistent vibrational bands, includ-

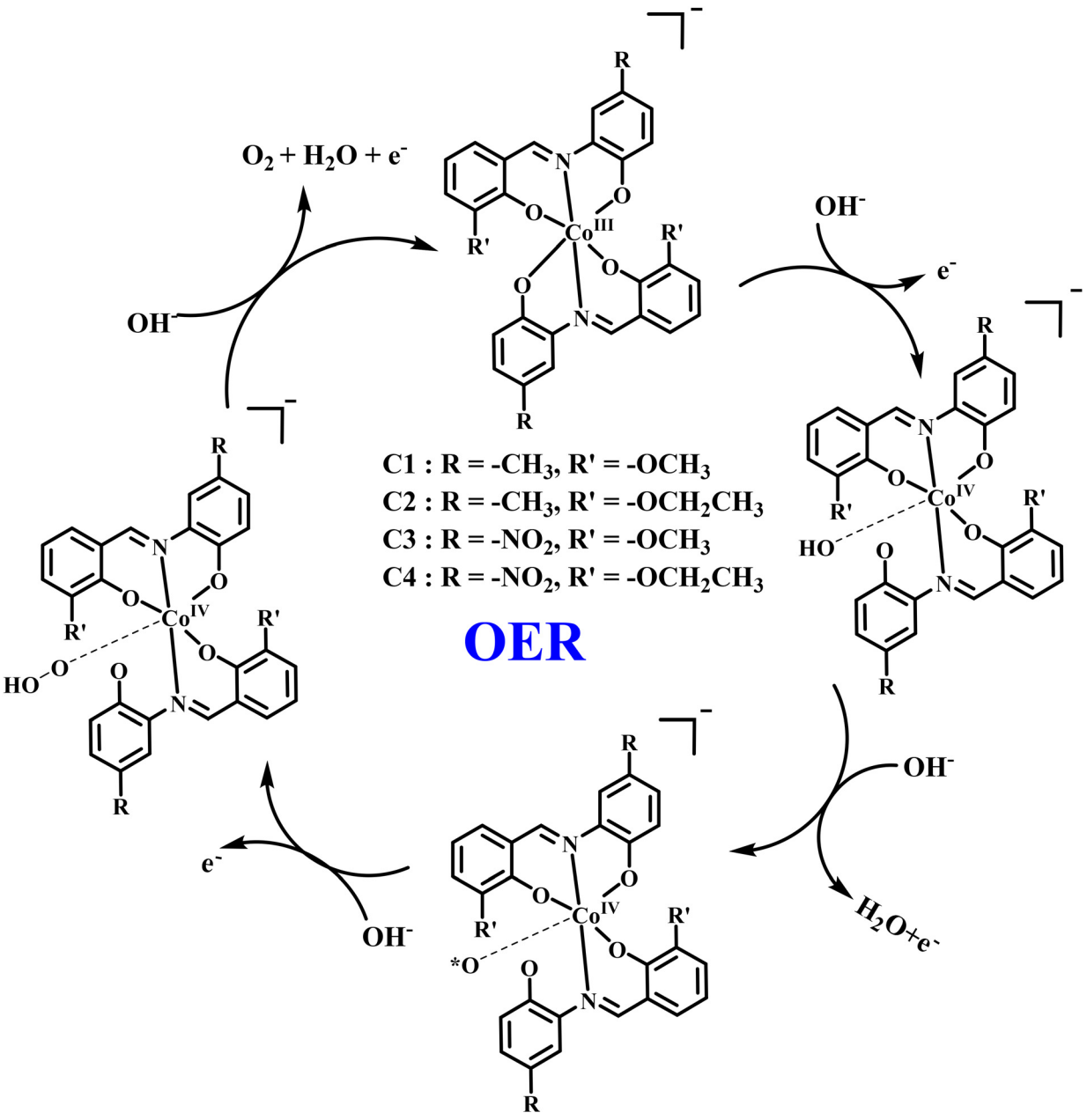

Scheme 2 Plausible OER mechanism catalyzed by complexes **C1**, **C2**, **C3**, and **C4** in an alkaline medium.

Table 3 Comparative summary of recently reported cobalt-based heterogeneous OER catalysts in a KOH electrolyte

S. no.	Electrocatalyst	Electrolyte	Overpotential (mV)	Tafel slope (mV dec^{-1})	Current density (mA cm^{-2})	Ref.
1	$[(3,5\text{-Lutidine})_2Co(OAc)_2(H_2O)_2]$	1 M KOH	410	45.7	10	68
2	Co_2(*trans*-cinnamate)$_4$(2-aminopyrimidine)$_2(H_2O)$	0.1 M KOH	386	64	10	69
3	$[Co_3(L')2(\mu\text{-}\eta^1\text{:}\eta^1\ OAc)_2(CH_3CN)_2]$[a]	1 M KOH	380	58	10	46
4	$[Co_4(L')_2(\mu\text{-}\eta^1\text{:}\eta^1\text{-}OAc)_2(\eta^2\text{-}OAc)_2]\cdot 1.5CH_3OH\cdot 1.5\ CHCl_3$[a]	1 M KOH	325	85	10	47
5	$[Co\{(SeP^iPr_2)_2N\}_2]$	1 M KOH	320	61.6	10	51
6	Co_3O_4/graphene oxide	1 M KOH	415	91	10	70
7	CoP	1 M KOH	400	57	10	71
8	$[Co_{1.5}(tib)(dcpna)]\cdot 6H_2O$ MOF	1 M KOH	360	89	10	72
9	**C1**	1 M KOH	390	95	10	This work
10	**C2**	1 M KOH	370	71	10	This work
11	**C3**	1 M KOH	362	68	10	This work
12	**C4**	1 M KOH	340	63	10	This work

[a] L′ represents 2,2′-(((1*E*,1′*E*)-pyridine-2,6-diylbis(methanylylidene))bis(azanylylidine)diphenol).

ing the characteristic –CH═N– stretch, confirming that the key ligand–metal coordination framework remains intact. A comparative analysis of the experimental results indicates that XPS, SEM, PXRD, UV-vis, and FT-IR results of **C4** before and after OER studies remain largely unchanged, demonstrating that the catalyst retains its structural integrity and chemical composition after prolonged OER operation. These results revealed the stability of the **C4** complex in 1 M KOH solution. The plausible OER mechanism of this reaction is illustrated in Scheme 2. The oxygen evolution reaction (OER) occurring at the electrode surface is a complex, multistep electrochemical process. Under alkaline conditions, the OER is generally considered to proceed through four consecutive proton-coupled electron transfer (PCET) steps, involving the stepwise oxidation of hydroxide ions (OH^-) at the metal active center, ultimately leading to the evolution of molecular oxygen.[65]

$$OH^- + M* \rightarrow M*OH + e^- \quad \text{(i)}$$

$$M*OH + OH^- \rightarrow M*O + H_2O + e^- \quad \text{(ii)}$$

$$M* + OH^- \rightarrow M*OOH + e^- \quad \text{(iii)}$$

$$M*OOH + OH^- \rightarrow M* + H_2O + O_2 + e^- \quad \text{(iv)}$$

where M* refers to the active sites of the cobalt complexes.

In the case of the cobalt complex, the proposed mechanism may be summarized as follows. Initially, one of the aminophenolate oxygen donors of the Schiff base ligand might undergo partial decoordination from the Co center, thereby generating an open coordination site (M*).[66] This vacant site could then be occupied by a hydroxide ion, accompanied by the oxidation of Co(III) to Co(IV) with the release of one electron. In the subsequent step, a second OH^- ion likely attacks the coordinated OH ligand on the Co(IV) center, producing a surface-bound $O^\bullet$ radical species, one water molecule, and another electron. The nucleophilic attack of a third OH^- could lead to the formation of a Co–OOH intermediate, along with the third electron transfer. Finally, the attack of a fourth OH^- on the Co–OOH species may result in O_2 evolution, the generation of another H_2O molecule, the release of the fourth electron, and regeneration of the initial Co(III) complex.[67]

Furthermore, a comparison of our catalysts with recently reported cobalt catalysts as heterogeneous OER catalysts in KOH electrolytes is presented in Table 3. This comparison indicates that our catalysts demonstrate superior performance compared to other reported cobalt electrocatalysts.

Experimental section

Materials and methods

Compounds 2-amino-4-methylphenol and 2-amino-4-nitrophenol were purchased from Sigma Aldrich, 3-methoxy-salicylaldehyde and 3-ethoxy-salicylaldehyde from TCI, and $Co(CH_3COO)_2\cdot 6H_2O$ and triethylamine from Loba Chemie and were used for the preparation of ligands and the corresponding metal complexes. Solvents were purchased from Thomas Baker, doubly distilled, and used for experiments. ^{1}H NMR and ^{13}C NMR data were recorded on a Bruker Avance Neo 400 MHz instrument, where tetramethylsilane (TMS) was used as the internal standard. The samples were dissolved in deuterated DMSO-d_6 solvent, and chemical shifts were denoted in parts per million (ppm). Mass analysis of the compounds was conducted with the help of an Agilent 6530 LC/Q–TOF mass analyzer. UV-visible experiments were carried out on a JASCO V-630 UV-visible spectrometer in the wavelength range of 200–700 nm. Quartz cuvettes with a path length of 1.0 cm were used to record the absorption spectra. The FT-IR spectra of the compounds were recorded using a JASCO FTIR-4100 Fourier-Transform Infrared Spectrometer. Elemental analysis was performed on a PerkinElmer 2400 Series CHNS Analyser. XPS measurements were conducted using an ESCALAB 250Xi X-ray photoelectron spectrometer (Germany). SEM images were taken using a Carl Zeiss Evo 18 Environmental scanning electron microscope. The OER studies were conducted using the electrochemical workstation AURT-M204. Powder XRD measurements were carried out on a PANalytical XPERT-3 diffractometer system.

X-ray data collection and structural determination

Single-crystal X-ray diffraction data were collected at 295 K using a BRUKER APEX II diffractometer equipped with a CCD area detector and monochromatic Mo Kα radiation (λ = 0.7107 Å) with a graphite monochromator. Data acquisition, processing, and structure solution/refinement were carried out using SMART APEX software. Absorption corrections were applied using the SADABS program. Hydrogen atoms were positioned at the calculated locations and refined isotropically using a riding model. Details of the structural determination, crystallographic data, and refinement parameters are provided in Table S1. The CCDC deposition numbers for the complexes are as follows: **C1** (2450219), **C2** (2450220), **C3** (2450221), and **C4** (2450222).

Synthesis of ligands $L1H_2$–$L4H_2$

The ligands were synthesized *via* a simple condensation reaction between 2-amino-substituted phenols and substituted salicylaldehydes in ethanol. The reaction mixture was refluxed for 4 h, yielding a red precipitate. The precipitate was filtered, washed with cold ethanol, and dried under vacuum. The synthetic details for each ligand are provided below.

Synthesis of $L1H_2$

The ligand was synthesized by adopting a modified literature method.[73] A solution of 2-amino-4-methylphenol (1.0 g, 1.0 mmol) and 3-methoxysalicylaldehyde (1.24 g, 1.0 mmol) in 20 mL of ethanol was refluxed for 4 h. The red precipitate obtained was filtered, washed with ethanol, and dried under vacuum. Yield: 1.92 g (92%).

Anal. calcd (%) for $C_{15}H_{15}NO_3$ (**$L1H_2$**): C, 70.02; H, 5.88; N, 5.44. Found (%): C, 70.01; H, 5.83; N, 5.39. ^{1}H NMR (400 MHz, DMSO-d_6, δ ppm): 14.13 (s, 1H), 9.55 (s, 1H), 8.95 (s, 1H), 7.20–7.19 (m, 1H), 7.17 (s, 1H), 7.06 (d, 1H, J = 8 Hz), 6.94–6.92 (dd, 1H), 6.86–6.84 (dd, 2H), 3.80 (s, 3H), 2.25 (s, 3H). ^{13}C NMR (100 MHz, DMSO-d_6, δ ppm): 161.18, 152.03, 148.74, 148.23, 133.93, 128.54, 128.37, 123.79, 119.70, 119.23, 117.88, 116.38, 115.10, 55.83, 20.20. UV-vis [MeCN: λ_{max}, nm (ε, L mol^{-1} cm^{-1}): 347 (13 800), 274 (14 500)].

Synthesis of $L2H_2$

A solution of 2-amino-4-methylphenol (1.0 g, 1.0 mmol) and 3-ethoxy-salicylaldehyde (1.35 g, 1.0 mmol) in 20 mL of ethanol was refluxed for 4 h. The red precipitate obtained was filtered, washed with ethanol, and dried under vacuum. Yield: 1.98 g (90%).

Anal. calcd (%) for $C_{16}H_{17}NO_3$ (**$L2H_2$**): C, 70.83; H, 6.32; N, 5.16. Found (%): C, 70.81; H, 6.29; N, 5.14. ^{1}H NMR (400 MHz, DMSO-d_6, δ ppm): 14.18 (s, 1H), 9.55 (s, 1H), 8.95 (s, 1H), 7.21 (s, 1H), 7.18–7.16 (dd, 1H), 7.06–7.04 (dd, 1H), 6.94–6.92 (dd, 1H), 6.87–6.80 (m, 2H), 4.06 (q, 2H), 2.25 (s, 3H), 1.34 (t, 3H, J = 8 Hz). ^{13}C NMR (100 MHz, DMSO-d_6, δ ppm): 161.16, 152.29, 148.80, 147.33, 133.87, 128.54, 128.35, 123.95, 119.64, 119.36, 117.88, 116.51, 116.39, 64.05, 20.20, 14.84. UV-vis [MeCN: λ_{max}, nm (ε, L mol^{-1} cm^{-1}): 348 (14 700), 275 (15 400)].

Synthesis of $L3H_2$

A solution of 2-amino-4-nitrophenol (1.0 g, 1 mmol) and 3-methoxysalicylaldehyde (1.1 g, 1 mmol) in ethanol was refluxed for 4 h. The red precipitate obtained was filtered, washed with ethanol, and dried under vacuum. Yield: 1.70 g (91%). Anal. calcd (%) for $C_{14}H_{12}N_2O_5$ (**$L3H_2$**): C, 58.33; H, 4.20; N, 9.72. Found (%): C, 58.29; H, 4.18; N, 9.70. ^{1}H NMR (400 MHz, DMSO-d_6, δ ppm): 13.41 (s, 1H), 11.42 (s, 1H), 9.09 (s, 1H), 8.28 (d, 1H), 8.08–8.05 (dd, 1H), 7.28–7.23 (m, 2H), 7.12 (d, 1H, J = 4 Hz), 6.90 (t, 1H), 3.82 (s, 3H). ^{13}C NMR (100 MHz, DMSO-d_6, δ ppm): 164.48, 157.65, 151.15, 148.07, 139.98, 135.45, 124.10, 123.81, 120.15, 118.48, 116.35, 115.33, 113.11, 56.20. UV-vis [MeCN: λ_{max}, nm (ε, L mol^{-1} cm^{-1}): 289 (23 150), 224 (32 750)].

Synthesis of $L4H_2$

A solution of 2-amino-4-nitrophenol (1.0 g, 1 mmol) and 3-ethoxysalicylaldehyde (1.1 g, 1 mmol) in ethanol was refluxed for 4 h. The red precipitate obtained was filtered, washed with ethanol, and dried under vacuum. Yield: 1.78 g (91%). Anal. calcd (%) for $C_{15}H_{14}N_2O_5$ (**$L4H_2$**): C, 59.60; H, 4.67; N, 9.27. Found (%): C, 59.57; H, 4.65; N, 9.23. ^{1}H NMR (400 MHz, DMSO-d_6, δ ppm): 13.46 (s, 1H), 11.42 (s, 1H), 9.10 (s, 1H), 8.30 (d, 1H, J = 4 Hz), 8.09–8.06 (dd, 1H), 7.28–7.23 (m, 1H), 7.14–7.11 (m, 2H), 6.90–6.86 (m, 1H), 4.08 (q, 2H), 1.35 (t, 3H, J = 8 Hz). ^{13}C NMR (100 MHz, DMSO-d_6, δ ppm): 164.56, 157.89, 151.48, 147.50, 140.26, 140.01, 137.66, 124.33, 120.57, 119.44, 118.88, 113.16, 107.64, 64.46, 14.61. UV-vis [MeCN: λ_{max}, nm (ε, L mol^{-1} cm^{-1}): 272 (20 300), 224 (28 700)].

Synthesis of complexes C1–C4

A general procedure was adopted for the synthesis of all four complexes.

[Co(III)$(L1)_2$]$Et_3NH{\cdot}2H_2O$ (C1). $L1H_2$ (0.103 g, 0.2 mmol) was dissolved in 10 mL of methanol, and an excess of triethylamine (TEA) was added. The reaction mixture was stirred for 10 minutes, followed by the addition of $Co(CH_3COO)_2{\cdot}6H_2O$ (0.050 g, 0.1 mmol). Stirring was continued for 6 h, and then the solution was filtered and left to undergo slow evaporation. After three days, brown-colored crystals suitable for X-ray diffraction analysis were obtained.

Yield: 102 mg (72%). Anal. calcd (%) for $C_{36}H_{46}CoN_3O_8$: C, 61.10; H, 6.55; N, 5.94. Found (%): C, 61.07; H, 6.53; N, 5.92. ^{1}H NMR (400 MHz, DMSO-d_6, δ ppm): 8.84 (s, 2H), 7.97 (s, 2H), 7.21 (d, 2H, J = 8 Hz), 6.67 (d, 2H, J = 8 Hz), 6.49 (d, 2H, J = 8 Hz), 6.32 (d, 4H, J = 8 Hz), 3.78 (br s, 12H), 2.71 (br s, 1H), 2.34 (s, 6H), 1.00 (t, 9H, J = 4 Hz). HRMS for $C_{30}H_{30}CoN_2O_8{\cdot}C_6H_{15}NH$: calcd: m/z = 707.69, obtained: m/z: 707.1021. UV-vis [MeCN: λ_{max}, nm (ε, L mol^{-1} cm^{-1}): 431 (9200), 247 (33 650)].

[Co(III)$(L2)_2$]$Et_3NH{\cdot}2H_2O$ (C2). $L2H_2$ (0.050 g, 0.2 mmol) was dissolved in 10 mL of methanol, and an excess of triethylamine (TEA) was added. The mixture was stirred for 10 minutes, followed by the addition of $Co(CH_3COO)_2{\cdot}6H_2O$ (0.023 g, 0.1 mmol). Stirring was continued for 6 h and then

the solution was filtered and left to undergo slow evaporation. After three days, brown-colored crystals suitable for X-ray diffraction analysis were obtained.

Yield: 103 mg (70%). Anal. calcd (%) for $C_{38}H_{50}CoN_3O_8$: C, 62.03; H, 6.85; N, 5.71. Found (%): C, 62.01; H, 6.81; N, 5.68. ^{1}H NMR (400 MHz, DMSO-d_6, δ ppm): 8.87 (s, 2H), 7.99 (s, 2H), 7.28 (d, 2H, J = 8 Hz), 6.73 (d, 2H, J = 8 Hz), 6.57 (d, 2H, J = 4 Hz), 6.39 (d, 2H, J = 8 Hz), 6.32 (t, 2H, J = 8 Hz), 3.74 (br s, 6H), 3.45 (q, 4H), 2.71 (br s, 1H), 2.38 (s, 6H), 1.00 (t, 9H, J = 8 Hz), 0.80 (t, 6H, J = 8 Hz). HRMS for $C_{32}H_{34}CoN_2O_8{\cdot}C_6H_{15}NH$ calcd: m/z = 735.74, obtained: m/z: 735.1625. UV-Vis [MeCN: λ_{max}, nm (ε, L mol^{-1} cm^{-1}): 449 (7700), 258 (22 650)].

[Co(III)(L3)$_2$]Et$_3$NH·H$_2$O (C3). **L3H$_2$** (0.050 g, 0.2 mmol) was dissolved in 10 mL of a 1 : 1 acetonitrile–methanol mixture, and an excess of triethylamine (TEA) was added. The mixture was stirred for 10 minutes, followed by the addition of Co$(CH_3COO)_2{\cdot}6H_2O$ (0.023 g, 0.1 mmol). Stirring was continued for 6 h and then the solution was filtered and left to undergo slow evaporation. After three days, brown-colored crystals suitable for X-ray diffraction analysis were obtained.

Yield: 108 mg (71.52%). Anal. calcd (%) for $C_{34}H_{38}CoN_5O_{11}$: C, 54.33; H, 5.10; N, 9.32. Found (%): C, 54.29; H, 5.07; N, 9.28. ^{1}H NMR (400 MHz, DMSO-d_6, δ ppm): 9.17 (s, 2H), 9.09 (s, 2H), 7.73 (d, 2H, J = 8 Hz), 7.20 (d, 2H, J = 8 Hz), 6.42 (d, 2H, J = 8 Hz), 6.37 (d, 2H, J = 12 Hz), 6.27 (t, 2H, J = 8 Hz), 3.69 (br s, 12H), 2.32 (br s, 1H), 0.80 (t, 9H, J = 8 Hz). HRMS for $C_{32}H_{34}CoN_2O_8{\cdot}C_6H_{15}NH$ calcd: m/z = 751.62, obtained: m/z: 751.1456. UV-vis [MeCN: λ_{max}, nm (ε, L mol^{-1} cm^{-1}): 422 (21 950), 256 (37 850)].

[Co(III)(L4)$_2$]Et$_3$NH (C4). **L4H$_2$** (0.050 g, 0.2 mmol) was dissolved in 10 mL of a 1 : 1 acetonitrile–methanol mixture, and an excess of triethylamine (TEA) was added. The mixture was stirred for 10 minutes, followed by the addition of $Co(CH_3COO)_2{\cdot}6H_2O$ (0.023 g, 0.1 mmol). Stirring was continued for 6 hours and then the solution was filtered and left to undergo slow evaporation. After three days, dark brown-colored crystals suitable for X-ray diffraction analysis were obtained.

Yield: 110 mg (71.90%). Anal. calcd (%) for $C_{36}H_{40}CoN_5O_{10}$: C, 56.77; H, 5.29; N, 9.19. Found (%): C, 56.72; H, 5.26; N, 9.15. ^{1}H NMR (400 MHz, DMSO-d_6, δ ppm): 9.29 (s, 2H), 9.18 (d, 2H, J = 4 Hz), 7.85 (dd, 2H), 7.39 (dd, 2H), 6.59 (dd, 2H), 6.53 (d, 2H, J = 8 Hz), 6.37 (t, 2H, J = 8 Hz), 3.38 (q, 4H), 3.18 (br s, 1H), 2.88 (q, 6H,) 1.07 (t, 9H, J = 8 Hz), 0.72 (t, 6H, J = 4 Hz). HRMS for $C_{32}H_{34}CoN_2O_8{\cdot}C_6H_{15}NH$ calcd: m/z = 735.74, obtained: m/z:735.1625. UV-vis [MeCN: λ_{max}, nm (ε, L mol^{-1} cm^{-1}): 427 (28 800), 258 (43 750)].

Conclusion

In summary, four new homoleptic Co(III) complexes were successfully synthesized *via* aerial oxidation of Co(II) using Schiff bases derived from 2-amino-substituted phenols and substituted salicylaldehydes as ligands. Single-crystal X-ray diffraction (SCXRD) analysis confirmed that all Co(III) complexes were obtained as mononuclear anionic units with triethylammonium ions as counter cations. The synthesised Co complexes (**C1**, **C2**, **C3** and **C4**) showed promising OER activity in 1 M KOH solution. The complex **C4** exhibited the best electrocatalytic performance, achieving a notably low overpotential of 340 mV *vs.* RHE and a lower Tafel slope of 63 mV dec^{-1}, suggesting faster electron transfer kinetics. The exceptional activity of **C4** can be attributed to the modulation of the ligand's electronic environment, where the synergistic interaction effect of electron-donating and electron-withdrawing groups with the Co(III) center enhanced the activity *via* charge transfer processes and intermediate stabilization. Structural and morphological analyses using XPS and SEM conducted both before and after OER operation confirmed that the oxidation state, chemical environment, and surface integrity of **C4** remain largely unchanged, emphasizing its stability during catalysis. Importantly, this study highlights the significance of rational ligand design for tuning the electrocatalytic behaviour of Co(III) complexes by modulating the functionality of the ligand framework. These results indicate that the incorporation of mixed electronic effects into ligand frameworks offers a promising strategy for the future development of efficient, low-cost molecular electrocatalysts. Further studies aimed at extending this ligand engineering approach to other first-row transition metals (*e.g.* Ni, Fe) and integrating these complexes into hybrid materials could unlock new opportunities for practical applications in water splitting and renewable energy technologies.

Author contributions

Janardhanan Aiswarya: formal analysis, data curation, visualization, validation, and writing – original draft. Ragunath Madhu: data curation, validation, and writing – original draft. Ottoor Anitha: data curation, visualization, and validation. Jan Grzegorz Malecki: validation and formal analysis. Subrata Kundu: supervision, visualization, writing – original draft, and writing & editing. Balasubramanian Murugesapandian: supervision, visualization, writing – original draft, writing & editing, project administration, and funding acquisition.

Conflicts of interest

The authors declare that they have no known competing financial interests or personal relationships that could have appeared to influence the work reported in this paper.

Data availability

Data will be made available on request.

Supplementary information is available. Supplementary information contains NMR, UV-vis, FT-IR, HRMS, XPS and other datas are available. See DOI: **https://doi.org/10.1039/d5dt01680k**.

CCDC 2450219–2450222 for (**C1–C4**) contain the supplementary crystallographic data for this paper.[74a–d]

Acknowledgements

J. A. acknowledges the Department of Science and Technology (DST) for an Inspire Fellowship (IF190958). R. M. acknowledges the Department of Science and Technology (DST) for an Inspire Fellowship. B. M. thanks the UGC, New Delhi, India, for the UGC FRP faculty award [F.4-5(94-FRP)/2014(BSR)] and SERB, New Delhi, India (CRG/2023/004394), for financial assistance. The authors acknowledge the NMR facility, CIC, Bharathiar University, supported by the DST PURSE Phase-II program. CSIR-CECRI Manuscript number : CECRI/PESVC/Pubs./2025-060.

References

1 S. Chu and A. Majumdar, *Nature*, 2012, **488**, 294–303.
2 B. M. Hunter, H. B. Gray and A. M. Muller, *Chem. Rev.*, 2016, **116**, 14120–14136.
3 L. Duan, A. Fischer, Y. Xu and L. Sun, *J. Am. Chem. Soc.*, 2009, **131**, 10397–10399.
4 S. Li, X. Hao, A. Abudula and G. Guan, *J. Mater. Chem. A*, 2019, **7**, 18674–18707.
5 Y. Song, C. Yu, D. Ma and K. Liu, *Coord. Chem. Rev.*, 2024, **499**, 215492.
6 B. Zhu, D. Xia and R. Zou, *Coord. Chem. Rev.*, 2018, **376**, 430–448.
7 N. Wen, X. Jiao, Y. Xia and D. Chen, *Mater. Chem. Front.*, 2023, **7**, 4833–4864.
8 Y. Zheng, L. Zhang, H. Huang, F. Wang, L. Yin, H. Jiang, D. Wang, J. Yang and G. Zuo, *Int. J. Hydrogen Energy*, 2019, **44**, 27465–27471.
9 N. Hassan, A. Jalil, S. Rajendran, N. Khusnun, M. Bahari, A. Johari, M. Kamaruddin and M. Ismail, *Int. J. Hydrogen Energy*, 2024, **52**, 420–441.
10 B. You and Y. Sun, *Acc. Chem. Res.*, 2018, **51**, 1571–1580.
11 Y. Jiao, Y. Zheng, M. Jaroniec and S. Z. Qiao, *Chem. Soc. Rev.*, 2015, **44**, 2060–2086.
12 Y. P. Zhu, C. Guo, Y. Zheng and S.-Z. Qiao, *Acc. Chem. Res.*, 2017, **50**, 915–923.
13 A. Vazhayil, L. Vazhayal, J. Thomas and N. Thomas, *Appl. Surf. Sci. Adv.*, 2021, **6**, 100184.
14 Z. Abdi, S. Nandy, K. H. Chae and M. M. Najafpour, *Inorg. Chem.*, 2021, **61**, 464–473.
15 M. Carmo, D. L. Fritz, J. Mergel and D. Stolten, *Int. J. Hydrogen Energy*, 2013, **38**, 4901–4934.
16 D. K. Singh, V. Ganesan, D. K. Yadav and M. Yadav, *Cryst. Growth Des.*, 2020, **20**, 6321–6328.
17 M. C. Kim and S. Y. Lee, *Chem. – Asian J.*, 2018, **13**, 334–341.
18 C. C. McCrory, S. Jung, I. M. Ferrer, S. M. Chatman, J. C. Peters and T. F. Jaramillo, *J. Am. Chem. Soc.*, 2015, **137**, 4347–4357.
19 S. Berardi, S. Drouet, L. Francas, C. Gimbert-Suriñach, M. Guttentag, C. Richmond, T. Stoll and A. Llobet, *Chem. Soc. Rev.*, 2014, **43**, 7501–7519.
20 R. Matheu, M. Z. Ertem, C. Gimbert-Surinach, X. Sala and A. Llobet, *Chem. Rev.*, 2019, **119**, 3453–3471.
21 X.-P. Zhang, A. Chandra, Y.-M. Lee, R. Cao, K. Ray and W. Nam, *Chem. Soc. Rev.*, 2021, **50**, 4804–4811.
22 Q.-F. Chen, Y.-H. Guo, Y.-H. Yu and M.-T. Zhang, *Coord. Chem. Rev.*, 2021, **448**, 214164.
23 J. Li, R. Guttinger, R. More, F. Song, W. Wan and G. R. Patzke, *Chem. Soc. Rev.*, 2017, **46**, 6124–6147.
24 P. Garrido-Barros, C. Gimbert-Surinach, R. Matheu, X. Sala and A. Llobet, *Chem. Soc. Rev.*, 2017, **46**, 6088–6098.
25 Y. Liu, D. Zhou, T. Deng, G. He, A. Chen, X. Sun, Y. Yang and P. Miao, *ChemSusChem*, 2021, **14**, 5359–5383.
26 S. Anantharaj, S. Ede, K. Karthick, S. S. Sankar, K. Sangeetha, P. Karthik and S. Kundu, *Energy Environ. Sci.*, 2018, **11**, 744–771.
27 M. Sun, R. Ge, S. Li, L. Dai, Y. Li, B. Liu and W. Li, *J. Energy Chem.*, 2024, **91**, 453–474.
28 S. Biswas, S. Bose, J. Debgupta, P. Das and A. N. Biswas, *Dalton Trans.*, 2020, **49**, 7155–7165.
29 X. Zhang, L. Wang, Y. Xie and H. Fu, *Coord. Chem. Rev.*, 2025, **533**, 216560.
30 C. He, L. Yang, J. Wang, T. Wang, J. Ju, Y. Lu and W. Chen, *Carbon Energy*, 2024, **6**, e573.
31 Y. Kang, Y. He, D. Pohl, B. Rellinghaus, D. Chen, M. Schmidt, V. Süß, Q. Mu, F. Li and Q. Yang, *ACS Appl. Mater. Interfaces*, 2022, **14**, 19324–19331.
32 F. T. Haase, A. Bergmann, T. E. Jones, J. Timoshenko, A. Herzog, H. S. Jeon, C. Rettenmaier and B. R. Cuenya, *Nat. Energy*, 2022, **7**, 765–773.
33 B. Paul, P. Bhanja, S. Sharma, Y. Yamauchi, Z. A. Alothman, Z.-L. Wang, R. Bal and A. Bhaumik, *J. Colloid Interface Sci.*, 2021, **582**, 322–332.
34 X. Guo, X. Liu, M. Wang, J. Yan, Y. Chen and S. Liu, *Small*, 2023, **19**, 2206695.
35 F. Lyu, Y. Bai, Q. Wang, L. Wang, X. Zhang and Y. Yin, *Dalton Trans.*, 2017, **46**, 10545–10548.
36 B. Zhang, J. Zhang, X. Tan, D. Tan, J. Shi, F. Zhang, L. Liu, Z. Su, B. Han and L. Zheng, *Chem. Commun.*, 2018, **54**, 4045–4048.
37 S. Y. Chae, Y. J. Hwang, J.-H. Choi and O.-S. Joo, *Electrochim. Acta*, 2013, **114**, 745–749.
38 B. V. Krishna, O. R. Ankinapalli, A. R. Reddy and J. S. Yu, *Small*, 2024, **20**, 2311176.
39 S. B. Kale, A. C. Lokhande, R. B. Pujari and C. D. Lokhande, *J. Colloid Interface Sci.*, 2018, **532**, 491–499.
40 J.-B. Chen, J. Ying, Y.-X. Xiao, G. Tian, Y. Dong, L. Shen, S. I. Cordoba de Torresi, M. D. Symes, C. Janiak and X.-Y. Yang, *ACS Catal.*, 2023, **13**, 14802–14812.
41 G. Huang, Y. Huang, A. Ali, Z. Chen, P. K. Shen, B. J. Ni and J. Zhu, *Electron*, 2024, **2**, e58.
42 J. Chang, Y. Xiao, M. Xiao, J. Ge, C. Liu and W. Xing, *ACS Catal.*, 2015, **5**, 6874–6878.
43 M. Zhu, Y. Zhou, Y. Sun, C. Zhu, L. Hu, J. Gao, H. Huang, Y. Liu and Z. Kang, *Dalton Trans.*, 2018, **47**, 5459–5464.
44 P. Chen, K. Xu, Y. Tong, X. Li, S. Tao, Z. Fang, W. Chu, X. Wu and C. Wu, *Inorg. Chem. Front.*, 2016, **3**, 236–242.

45 X. Peng, C. Pi, X. Zhang, S. Li, K. Huo and P. K. Chu, *Sustainable Energy Fuels*, 2019, **3**, 366–381.
46 E. M. Manohar, S. Roy, S. Bandyopadhyay, M. Pal, S. Singh, V. Ganesan, R. Pełka, P. Konieczny, M. Rams, H. Choi, S. Tothadi and S. Das, *Cryst. Growth Des.*, 2024, **24**, 1032–1041.
47 E. M. Manohar, H. N. Dhandapani, S. Roy, R. Pełka, M. Rams, P. Konieczny, S. Tothadi, S. Kundu, A. Dey and S. Das, *Inorg. Chem.*, 2024, **63**, 4883–4897.
48 N. Kamboj and R. K. Metre, *Inorg. Chem.*, 2024, **63**, 9771–9785.
49 D. Basu, M. M. Allard, F. R. Xavier, M. J. Heeg, H. B. Schlegel and C. N. Verani, *Dalton Trans.*, 2015, **44**, 3454–3466.
50 H.-T. Shi, X.-X. Li, F.-H. Wu and W.-B. Yu, *Dalton Trans.*, 2017, **46**, 16321–16326.
51 I. M. Abdullahi, J. Masud, P.-C. Ioannou, E. Ferentinos, P. Kyritsis and M. Nath, *Molecules*, 2021, **26**, 945.
52 T. L. Yusuf, S. D. Oladipo, S. Zamisa, H. M. Kumalo, I. A. Lawal, M. M. Lawal and N. Mabuba, *ACS Omega*, 2021, **6**, 13704–13718.
53 A. O. Sobola and G. M. Watkins, *J. Chem. Pharm. Res.*, 2013, **5**, 147–154.
54 Y.-X. Tan, Z.-J. Zhang, Y. Liu, J.-X. Yu, X.-M. Zhu, D.-Z. Kuang and W.-J. Jiang, *J. Mol. Struct.*, 2017, **1149**, 874–881.
55 L. Wang and L. Wang, *Front. Chem.*, 2022, **10**, 996383.
56 M. Huang, L. Jiao, D. Ning, J. Yang, J. Xu and Q. Wu, *Inorg. Chim. Acta*, 2024, **566**, 122013.
57 M. Joshi and A. R. Choudhury, *Appl. Organomet. Chem.*, 2022, **36**(1), e6483.
58 P. K. Mudi, N. Bandopadhyay, M. Joshi, M. Shit, S. Paul, A. R. Choudhury and B. Biswas, *Inorg. Chim. Acta*, 2020, **505**, 119468.
59 S. Kundu, N. Diyali, S. Saha, M. Chettri, R. K. Mahato, S. K. Agrawalla, C. S. Purohit and B. Biswas, *Inorg. Chim. Acta*, 2024, **570**, 122161.
60 R. Madhu, A. Karmakar, P. Arunachalam, J. Muthukumar, P. Gudlur and S. Kundu, *J. Mater. Chem. A*, 2023, **11**, 21767–21779.
61 R. Madhu, A. Karmakar and S. Kundu, *Inorg. Chem.*, 2023, **62**, 2726–2737.
62 D. den Boer and D. G. Hetterscheid, *J. Am. Chem. Soc.*, 2023, **145**, 23057–23067.
63 T. E. Khalil, S. M. Soliman, N. A. Khalil, A. El-Faham, S. Foro and A. El-Dissouky, *Appl. Organomet. Chem.*, 2022, **36**, e6565.
64 J. S. Stevens, S. J. Byard, C. C. Seaton, G. Sadiq, R. J. Davey and S. L. Schroeder, *Phys. Chem. Chem. Phys.*, 2014, **16**, 1150–1160.
65 K. Biradha, A. Goswami and R. Moi, *Chem. Commun.*, 2020, **56**, 10824–10842.
66 N. Kumar, L. Wagh, S. Mehmood, A. K. Das and T. K. Ghorai, *ChemPlusChem*, 2025, 2500054.
67 A. Saini, C. Das, S. Rai, A. Guha, D. Dolui, P. Majumder and A. Dutta, *Iscience*, 2023, **26**, 108189.
68 D. Tanwar, P. Jain, D. Ahluwalia, A. Sudheendranath, S. P. Thomas, P. P. Ingole and U. Kumar, *RSC Adv.*, 2023, **13**, 24450–24459.
69 J. Lee, H. Shin, S. Geum, S. Lee, K. M. Ok, J. Do and S. J. Kwon, *Catalysts*, 2023, **13**, 507.
70 I. Abidat, E. Cazayus, L. Loupias, C. Morais, C. Comminges, T. Napporn, D. Portehault, O. Durupthy, A.-S. Mamede and C. Chanéac, *J. Electrochem. Soc.*, 2019, **166**, H94.
71 M. Liu and J. Li, *ACS Appl. Mater. Interfaces*, 2016, **8**, 2158–2165.
72 Q. Meng, J. Yang, S. Ma, M. Zhai and J. Lu, *Polymers*, 2017, **9**, 676.
73 D. Gurbuz, A. Cinarli, A. Tavman and A. S. Birteksoz, *Chin. J. Chem.*, 2012, **30**, 970–978.
74 (*a*) J. Aiswarya, R. Madhu, O. Anitha, J. G. Malecki, S. Kundu, B. Murugesapandian, CCDC 2450219: Experimental Crystal Structure Determination, 2025, DOI: **10.5517/ccdc.csd.cc2n7nbx**; (*b*) J. Aiswarya, R. Madhu, O. Anitha, J. G. Malecki, S. Kundu, B. Murugesapandian, CCDC 2450220: Experimental Crystal Structure Determination, 2025, DOI: **10.5517/ccdc.csd.cc2n7ncy**; (*c*) J. Aiswarya, R. Madhu, O. Anitha, J. G. Malecki, S. Kundu, B. Murugesapandian, CCDC 2450221: Experimental Crystal Structure Determination, 2025, DOI: **10.5517/ccdc.csd.cc2n7ndz**; (*d*) J. Aiswarya, R. Madhu, O. Anitha, J. G. Malecki, S. Kundu, B. Murugesapandian, CCDC 2450222: Experimental Crystal Structure Determination, 2025, DOI: **10.5517/ccdc.csd.cc2n7nf0**.